# Optical Dispersion Data Analysis of Single Crystal CH<sub>3</sub>NH<sub>3</sub>PbBr<sub>3</sub> for Optimized Perovskite Solar Cell Active Layer Absorptance

Christopher L. McCleese, <sup>1,2,\*</sup> Michael C. Brennan, <sup>1,3</sup> Nathan Episcopo, <sup>4</sup> Lirong Sun, <sup>1,3</sup> Nina Hong, <sup>5</sup> C. V. Ramana, <sup>4,6</sup> Tod A. Grusenmeyer<sup>1,</sup> and Peter R. Stevenson, <sup>1,\*</sup>

<sup>1</sup>Materials and Manufacturing Directorate, Air Force Research Laboratory, Wright-Patterson Air Force Base, Ohio, 45433, USA

<sup>2</sup>General Dynamics Information Technology, 5000 Springfield St. Suite 200, Dayton, Ohio, 45431, USA

<sup>3</sup>Azimuth Corporation, 2970 Presidential Drive, #200, Fairborn, Ohio, 45324, USA

<sup>4</sup>Center for Advanced Materials Research, University of Texas at El Paso, 500 W. University Ave., El Paso, Texas 79968, USA

<sup>5</sup>J.A. Woollam Company, 311 South 7th St. Lincoln, Nebraska, 68508, USA

<sup>6</sup>Department of Aerospace & Mechanical Engineering, University of Texas at El Paso, 500 W. University Ave., El Paso, Texas 79968, USA

\*Email: christopher.mccleese.1.ctr@us.af.mil

\*Email: peter.stevenson.2@us.af.mil

### **ABSTRACT**

Proper derivation of CH<sub>3</sub>NH<sub>3</sub>PbX<sub>3</sub> (CH<sub>3</sub>NH<sub>3</sub><sup>+</sup> = methyl ammonium or MA<sup>+</sup>; X<sup>-</sup> = Cl<sup>-</sup>, Br<sup>-</sup>, I<sup>-</sup>) optical constants is a critical step toward the development of high-performance electronic and optoelectronic perovskite devices. To date, the optical dispersion regimes at, above, and below the band gap of these materials have been inconsistently characterized by omitting or underapproximating anomalous spectral features (from ultraviolet to infrared wavelengths). In this report, we present the rigorous optical dispersion data analysis of single crystal MAPbBr<sub>3</sub> involving variable angle spectroscopic ellipsometry data appended with transmission intensity data. This approach yields a more robust derivation of MAPbBr3 optical constants (refractive index, n, and extinction coefficient, k) for both anomalous (absorptance) and normal (no absorptance) optical dispersion regimes. Using the derived optical constants for our MAPbBr<sub>3</sub> single crystals, illustrative modeled solar cell device designs are presented in relation to nonrealistic designs prepared using representative optical constants reported in the literature to date. In comparison, our derived optical dispersion data enables the modeled design of realistic planar perovskite solar cell (PSC) optical performance where the active layer (MAPbBr<sub>3</sub>) is optimized for maximum solar radiation absorption. We further demonstrate optimized modeled planar PSC designs with minimal parasitic optical absorptance in non-active PSC device layers resulting in improved performance at broad angles of incidence (approximately 0-70°). Our robust derivation of MAPbBr<sub>3</sub> optical properties is expected to impact the optical dispersion data analysis of all perovskite analogs and expedite targeted development of, for example, solar cell, light-emitting diode, photo and X-ray/γ-ray detector, and laser system technologies.

KEYWORDS: absorption coefficient, CH<sub>3</sub>NH<sub>3</sub>PbBr<sub>3</sub>, extinction coefficient, methylammonium lead trihalide, optical design, optical properties, perovskite solar cell, refractive index

### 1. INTRODUCTION

Hybrid organic-inorganic lead halide perovskites (i.e., methylammonium lead trihalide,  $CH_3NH_3PbX_3$  also known as  $MAPbX_3$ , where MA = methylammonium or  $CH_3NH_3$ , and X = Cl, Br, or I) have garnered significant attention involving electronic, optoelectronic, laser, lightemitting diode, photodetector, and X-ray/γ-ray detector device technologies. <sup>1–8</sup> This is largely due to tunable process-dependent compositions, structures, and morphologies resulting in a wide range of material characteristics, such as changes in the bandgap, carrier mobility, and exciton binding energy. Additionally, the potential for adaptable low-cost manufacturing (compared to state-ofthe-art commercial technologies) make perovskites appealing for high-production through-put and scale-up manufacturing advancements. However, material and device development challenges impact the broader adoption of perovskite material integration at scale—including stability and durability limitations, material quality and property performance reproducibility, environmental or defect degradation, induced toxicity, and controlled synthetic scale-up methodologies. 10-12 As such, it is common to observe a wide range of reported material properties that impact the electrical responses and optical characteristics of MAPbX<sub>3</sub>. Such structure-property-processing effects complicate electronic and optoelectronic device design and development optimization strategies for commercialization.<sup>11</sup>

The most prominent application focus for halide perovskites is the development of high-performance, low-cost solar cells. Hybrid organic-inorganic lead halide perovskite solar cells (PSCs) have been shown to achieve a power conversion efficiency (PCE) of over 25%,  $^{14-16}$  which rivals state-of-the-art high-performance silicon solar cells ( $\geq 25\%$  PCE). Tr,18 Critical to the development of PSCs are the optical properties (refractive index, n, and extinction coefficient, k) of the halide perovskite active layer, which describe the way materials interact with light and

subsequently function as a photovoltaic material. Proper derivation of perovskite optical constants enables the optimized design of efficient solar cells. <sup>19–21</sup> While there are many considerations when designing an exemplary PSC (e.g., compositional bandgap tuning, surface nano or microstructured light trapping, multilayer tandem cell architectures, and enhanced charge carrier extraction), perhaps the most important device consideration is the perovskite layer absorptance within the given solar cell architecture. <sup>20</sup> Perovskite optical absorptance in a solar cell device directly impacts the efficacy of solar radiation absorption for an engineered PSC and the resulting PCE. Successfully optimizing perovskite active layer optical absorptance necessitates solar cell optical coating design iterations using material optical constants derived from rigorous optical dispersion data analysis.

The n and k for MAPbX<sub>3</sub> have been observed to vary between representative processing methodologies to date. If such process-induced optical dispersion variation is ignored at the design stage, PSCs can exhibit undesired parasitic optical absorptance by non-perovskite (non-active) layers resulting in variable optical transmission, reflection, or haze-like characteristics within solar radiation bands of interest (i.e., ultraviolet = 300-400 nm, visible = 400-700 nm, and infrared = 700-2500 nm).<sup>22</sup> To our knowledge, no comprehensive experimentally appended optical dispersion data analysis to derive the optical constants of MAPbX<sub>3</sub> has been performed to include notable anomalous optical dispersion characteristics including the sharp band edge transition (bandgap ~539 nm) and methylammonium spectral overtones below the bandedge (observed around 1050-2500 nm). As such, the optical property determination of exemplary MAPbX<sub>3</sub> has been largely under approximated and, consequently, evokes uncertainty with respect to optical properties reported in prior work (discussed below).

Fundamental derivation of MAPbX<sub>3</sub> optical constants is paramount toward the development of high-performance electronic and optoelectronic perovskite devices.<sup>13,21</sup> In this report, we present a rigorous optical dispersion data analysis of single crystal MAPbBr<sub>3</sub> via variable angle spectroscopic ellipsometry appended with transmission intensity data. This results in a robust derivation of MAPbBr<sub>3</sub> optical constants for normal and anomalous optical dispersion regimes. Using the derived optical constants for our single crystal MAPbBr<sub>3</sub>, exemplary modeled solar cell optical device designs are optimized for perovskite layer absorptance. Our optimized PSC designs demonstrate improved optical performance in comparison to designs prepared using illustrative MAPbBr<sub>3</sub> literature optical constants reported to date.

### 2. EXPERIMENTAL SECTION

## 2.1. Preparation of Single Crystal MAPbBr<sub>3</sub>

The MAPbBr<sub>3</sub> crystals characterized in this work were grown following a modified inverse temperature crystallization (ITC) method reported in the literature.<sup>23</sup> An illustration of the growth process is shown in **Figure 1a**. A 1:1 molar ratio of PbBr<sub>2</sub> and MABr was dissolved in DMF. The precursor solution was allowed to stir at room temperature for 24 hours to ensure that all starting materials dissolved. The precursor solution was then passed through a 0.2 µm PTFE syringe filter and added directly to a glass crystallizing dish on a hot plate. Small seed crystals were grown in an initial crystal growth step. Once the seeds had grown to an appreciable size for ease of handling (~1×1×0.5 mm), they were harvested from the growth solution and transferred to a separate glass crystallizing dish containing fresh precursor solution for seeded growth propagation. Seeded crystal growth was performed on a glass substrate placed at the bottom of the crystallizing dish to

achieve a flat crystal surface at the glass-crystal interface. The growth was allowed to propagate for approximately five days uninterrupted. Once the growth was complete, a  $\sim 2.7 \times 2.7 \times 0.4$  cm crystal (**Figure 1b**) was removed from the solution and dried with a Kimwipe prior to further analysis. **Figure 1c** shows an illustration of the cubic MAPbBr<sub>3</sub> unit cell where the gray spheres at the center of the octahedra represent Pb<sup>2+</sup>, the green spheres on the corners represent the halide ( $X^-$ ), and the blue sphere at the center of the unit cell is the organic cation ( $A^+$ ).

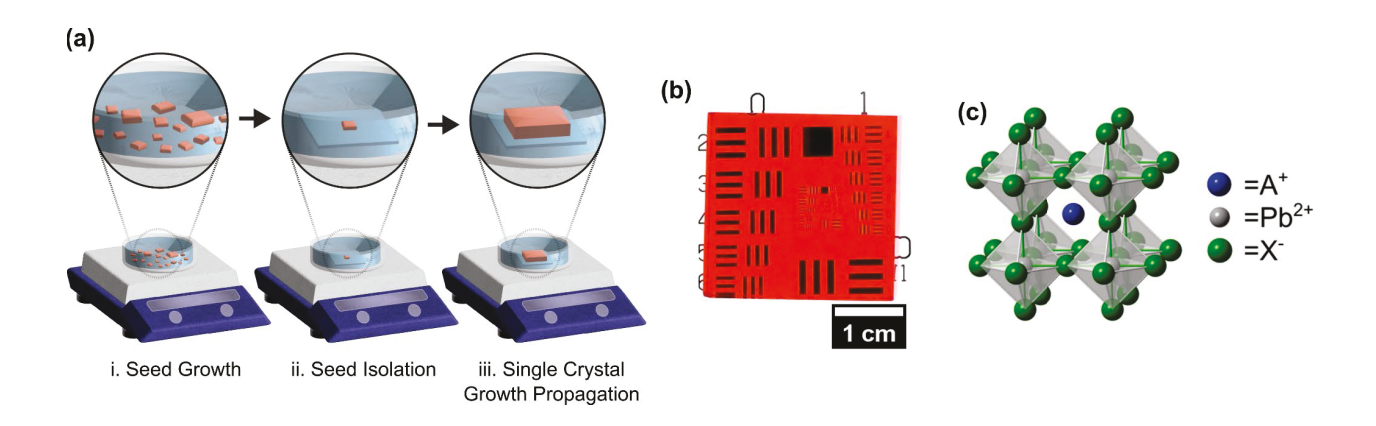


**Figure 1.** (a) Schematic of modified ITC growth of single crystal MAPbBr<sub>3</sub>. (b) Picture of single crystal MAPbBr<sub>3</sub> prepared via solvothermal synthesis shown in (a) on top of a United States Air Force 1951 test target. (c) Chemical structure of MAPbBr<sub>3</sub> cubic crystallographic phase unit cell.

### 2.2. X-Ray Diffraction

X-ray diffraction (XRD) measurements ( $\theta/2\theta$ ) were performed using a Rigaku Smartlab x-ray diffractometer with a Cu K<sub>\alpha</sub> source operating at 40 kV and 150 mA. XRD patterns were collected over the range of 5° to 60° 20. A channel-cut Ge (220) double-bounce monochromator

was used on the copper source side to strip the  $K\alpha_2$  and  $K_\beta$  X-ray lines. Measurements were done at room temperature and under ambient conditions. Single crystals were laid flat on the sample XRD holder so that diffraction patterns were acquired from the larger area surfaces.

### 2.3. Optical Profilometry

Root mean squared (RMS) surface roughness analysis was performed using a Bruker ContourX-500 3D Optical Profilometer equipped with dual color LED illumination (white light and 532 nm green light), automated objective turret with  $2.5\times$ ,  $5\times$ ,  $10\times$ ,  $20\times$ , and  $50\times$  objective apertures, and additional internal  $0.5-2\times$  zoom lens (for a maximum of  $100\times$ ). RMS surface roughness measurements were acquired via phase shift interferometry using the 532 nm illumination source in order to achieve sub-angstrom resolution. Measurements were acquired with the  $10\times$  objective and  $1\times$  internal zoom lens (xy pixel size of  $\sim$ 790 nm).  $1\times1$  mm area maps were constructed by stitching 6 separate images together with  $\sim$ 20% overlap with neighboring images. The data was analyzed with Vision64 software (Version 5.51). 2D interferometry maps were corrected for tilt, exported, and replotted in Origin.

### 2.4. X-Ray Photoelectron Spectroscopy

The chemical composition of a ~1 cm<sup>2</sup> cleaved piece of as-grown MAPbBr<sub>3</sub> was analyzed using a Thermo Scientific Escalab xi<sup>+</sup> X-ray Photoemission Spectrometer (XPS) equipped with a monochromatic X-ray source with an Al anode producing characteristic X-rays with photon energy of 1487 eV. The XPS spectrum was measured at the crystal surface that was in contact with the glass substrate during growth propagation. A survey scan was measured along with high resolution scans of Pb 4f, O 1s, N 1s, Br 3d, and C 1s core levels to evaluate the MAPbBr<sub>3</sub> chemical

composition on the sample surface. All spectra were collected without the use of a flood gun to neutralize the sample.

The XPS data was analyzed using CasaXPS processing software. All MAPbBr<sub>3</sub> XPS spectra were calibrated to the adventitious carbon on the sample surface used as a charge correction reference peak region with peak centered adjusted to 284.8 eV. The O 1s, C 1s, and Br 3d<sub>5/2</sub> 3d<sub>3/2</sub> high-resolution spectra backgrounds were treated with Tougaard function, a linear function was used for N 1s, and the core level Pb 4f<sub>7/2</sub> 4f<sub>5/2</sub> background was modeled with a Shirley function. Most of the synthetic peak models used a LA line shape—a numeric convolution of a Lorentzian with a Gaussian. Select peaks were modeled with the product of a Lorentzian and Gaussian (GL) to achieve a lower residual standard deviation.<sup>24</sup> Quantification of atomic concentration was calculated from a spectra formed by merging high-resolution core-level peaks, and integrating peak regions then normalizing the individual core level signal area to the total peak area yielding atomic percentage.

### 2.5. Energy Dispersive X-Ray Spectroscopy

Energy dispersive x-ray spectroscopy (EDS) was performed using a Zeiss Gemini 500 scanning electron microscope (SEM) operating at 20 keV which was equipped with an Oxford Instruments X-Max 80 detector. The spectrum was collected on the crystal surface that was in contact with the glass slide during growth. The atomic concentration was calculated using Oxford Instrument NanoAnalysis AZtec (Version 6.0) software.

### 2.6. Variable Angle Spectroscopic Ellipsometry and Spectrophotometry

Variable angle spectroscopic ellipsometry was carried out using an RC2 ellipsometer (JA Woollam). Reflection measurements were collected from 50-80° at 5° increments for wavelengths 200-2500 nm. Optical dispersion data analysis of the raw ellipsometry data was performed using CompleteEASE v6.55 (JA Woollam). An Agilent Cary 5000 UV-VIS-NIR spectrometer was used to collect the transmission intensity of the crystal at normal incidence from 200-2500 nm.

### 2.7. Modeled Solar Cell Optical Device Designs

OptiLayer v.15.12 was used to evaluate perovskite solar cell designs and optimize MAPbBr<sub>3</sub> active layer absorptance in representative design architectures. OptiLayer is a commercial optical coating design software that employs transfer matrix method modeling with custom optimization routines in the design of one-dimensional multilayer optical devices and coatings.

### 3. RESULTS AND DISCUSSION

3.1. Comparison of MAPbBr<sub>3</sub> Optical Properties and Impact on Perovskite Solar Cell
Active Layer Absorptance

A comparison of example MAPbBr<sub>3</sub> optical properties (refractive index, n, and extinction coefficient, k) reported in the literature is shown in **Figure 2**. The optical dispersions compared in **Figure 2** represent the optical properties of MAPbBr<sub>3</sub> grown using different antisolvent,  $^{25-27}$  hydrothermal,  $^{28}$  and ITC<sup>29</sup> growth methodologies. It is important to note that changes of  $\geq 0.1$  for either n or k are generally considered large. As such, a very large variation in optical dispersion behavior is observed for the illustrative literature values shown. These data are not meant to

represent a comprehensive comparison of all reported MAPbBr<sub>3</sub> optical constants to date—simply an illustrative representation of supposed n and k characteristics. For these data, a maximum  $\Delta n = 0.57$  ( $\Delta k = 0.34$ ) at the ~539 nm (~2.3 eV) bandgap, a maximum  $\Delta n = 0.80$  ( $\Delta k = 0.37$ ) above the bandgap, and a maximum  $\Delta n = 0.26$  ( $\Delta k = 0.35$ ) below the bandgap is observed. For comparison, Li et al. show a similarly large change in n and k for MAPbI<sub>3</sub> from different literature reports and attribute these to changes in crystallinity, density, surface roughness, impurities, point defects, and oxidative degradation.<sup>15</sup>

The magnitude of the  $\Delta n$  and  $\Delta k$  in **Figure 2** is unexpected assuming controlled MAPbBr<sub>3</sub> growth processing conditions and appropriate post-growth handling procedures. However, changes due to processing dependencies and surface or bulk material degradation have been shown to change the chemical composition and crystalline structure of MAPbX<sub>3</sub> that directly impact the associated optical properties.<sup>15</sup> Process-induced effects are known to generate lattice defects and dopant impurities while material degradation generally occurs due to unprotected, prolonged ambient air and moisture exposure under variable temperature fluctuation. <sup>10</sup> Defects and impurities within the crystalline lattice (such as lead or halide vacancies or interstitials) and surface degradation (such as oxidation) also affect the resulting optical properties of MAPbBr<sub>3</sub> primarily due to changes to the band gap (chemical composition), electron-hole pair recombination dynamics, and/or associated absorption/emission behavior. Additionally, as mentioned above, inaccurate modeling assumptions and the resulting robustness of the optical dispersion data analysis can potentially contribute to variability in the derived n and k (discussed in Section 3.3). Overall, we consider the wide range of responses in Figure 2 to be the result of both varying levels of surface and/or material quality (e.g., defect density, morphology, oxidation, surface roughness,

etc.) and the robustness of the fits employed to derive the optical properties of the given MAPbBr<sub>3</sub> material.

While a  $\geq$ 0.1 change in n and k for any material can result in significant optical device design discrepancy challenges, the  $\Delta k = 0.35$  below the band edge in **Figure 2b** is of specific concern for these representative MAPbBr<sub>3</sub> and expected PSC solar radiation absorption. Given a bandgap of  $\sim$ 539 nm, it is expected that k should rapidly approach zero at this wavelength and below. However, this is not the case for most reported values of k, except for Choi and coworkers. Here, again, the large  $\Delta k$  for MAPbBr<sub>3</sub> is likely due to differences in material surface quality (e.g., oxidation, doping, and/or surface roughness) in addition to inadequate optical dispersion data analysis to derive the reported values. Furthermore, the differences in the crystallographic face orientation responses reported by Tao and coworkers are likewise unexpected given MAPbBr<sub>3</sub> is not considered a birefringent material (exhibiting neither uniaxial or biaxial optical anisotropy).

When solar radiation interacts with a planar thin-film solar cell, the response of the light through a given device architecture is determined by the optical properties and thicknesses of each layer in the PSC stack. Here, we use an illustrative single junction planar solar cell architecture (five layers excluding the substrate) to demonstrate the impact of variable active layer perovskite n and k inputs on the modeled PSC optical performance: (i) encapsulating substrate, (ii) front contact, (iii) electron transport layer, (iv) active absorbing layer, (v) hole transport layer, and (vi) back contact. For simplicity, we use a similar device architecture as reported by Ball et al. (see **Figure 3a**) with MAPbBr<sub>3</sub> as the active layer.<sup>31</sup> Here, the substrate is glass (infinite modeled thickness), the front contact is fluorine-doped tin oxide (FTO, 420 nm thick), the electron transport layer is titanium dioxide (TiO<sub>2</sub>, 41 nm thick), the active absorbing layer is MAPbBr<sub>3</sub> (492 nm thick), the hole transport layer is 2.2'.7.7'-tetrakis-(N,N-di-4-methoxyphenylamino)-9.9'-

spirobifluorene (Spiro-OMeTAD, 253 nm thick), and the back contact is gold (Au, 30 nm thick). The optical properties for non-MAPbBr<sub>3</sub> device material layers can be found in Ref. [31].

Figure 3b shows the modeled absorptance of this device configuration using the different MAPbBr<sub>3</sub> n and k inputs from Figure 2. Here, for simplicity of illustration, the respective layer thicknesses for each material are fixed in the model as listed above. Figure 3c shows the individual MAPbBr<sub>3</sub> layer absorptance for comparison to the device in Figure 3b. Here, the percent absorptance is similar for each optical constant input from Figure 2; however, there is a distinct and significant deviation in optical absorptance at and below the bandgap for all modeled PSC devices due to the large  $\Delta n$  and  $\Delta k$  discussed. This deviation is further observed in the individual MAPbBr<sub>3</sub> layer absorptance shown in Figure 3c. Here, the active layer MAPbBr<sub>3</sub> optical absorptance is selectively compared in relation to the total PSC device absorptance shown in Figure 3b. Figure 3c suggests the primary contribution for the wide range in optical absorptance in Figure 3b is primarily due to the variable  $\Delta n$  and  $\Delta k$  from the MAPbBr<sub>3</sub> active layer. Figure 3b,c illustrate nonrealistic modeled optical absorptance in both the PSC device and active layer at and below the MAPbBr<sub>3</sub> bandgap (assuming minimal structure-property-processing material related effects).

While the MAPbBr<sub>3</sub>  $\Delta n$  and  $\Delta k$  from the reported literature responses predominantly contribute to the nonrealistic modeled optical absorptance, planar PSC device layer optimization (e.g., layer thicknesses and optical constants of the other device layers) can also contribute to the variable modeled optical performance. As such, it is likewise necessary to optimize the predicted optical performance of a given PSC involving the active layer absorptance performance and mitigate parasitic absorption from other device layers. In most cases, this can be carried out by simply optimizing the thickness-dependent (or path length of light) MAPbBr<sub>3</sub> active layer

absorptance with respect to the other material layers in the given device configuration. **Figure 3d** shows the difference in optical absorptance between optimized and unoptimized MAPbBr<sub>3</sub> active layer thickness PSC designs,

PSC  $\triangle A\%$  = Optimized PSC A% - Unoptimized PSC A%, (Eq. 1)

while **Figure 3e** shows the difference in optical absorptance between only the MAPbBr<sub>3</sub> layers for the optimized and unoptimized PSC designs (i.e., all other device layers are fixed in thickness as discussed above),

MAPbBr $_3$  Layer  $\Delta A\%$  = Optimized MAPbBr $_3$  Layer A% - Unoptimized MAPbBr $_3$  Layer A%. (Eq. 2)

These modeled results illustrate minor, yet significant, improvement in absorptance slightly above the MAPbBr<sub>3</sub> bandgap (**Figure 3d,e**). In contrast, this simple optimized design attempt in MAPbBr<sub>3</sub> active layer optical absorptance yields drastic deviations at and below the bandgap that are likewise considered nonrealistic (also compare responses below the MAPbBr<sub>3</sub> bandgap in **Figure 3b,c**). Consequently, a more robust derivation of MAPbBr<sub>3</sub> optical constants is first required to establish baseline PSC design optical performance prior to designing optimized device configurations. Our approach to derive robust optical constants for MAPbBr<sub>3</sub> is discussed below for representative high-quality single crystal MAPbBr<sub>3</sub> along with associated morphological and chemical composition characteristics.

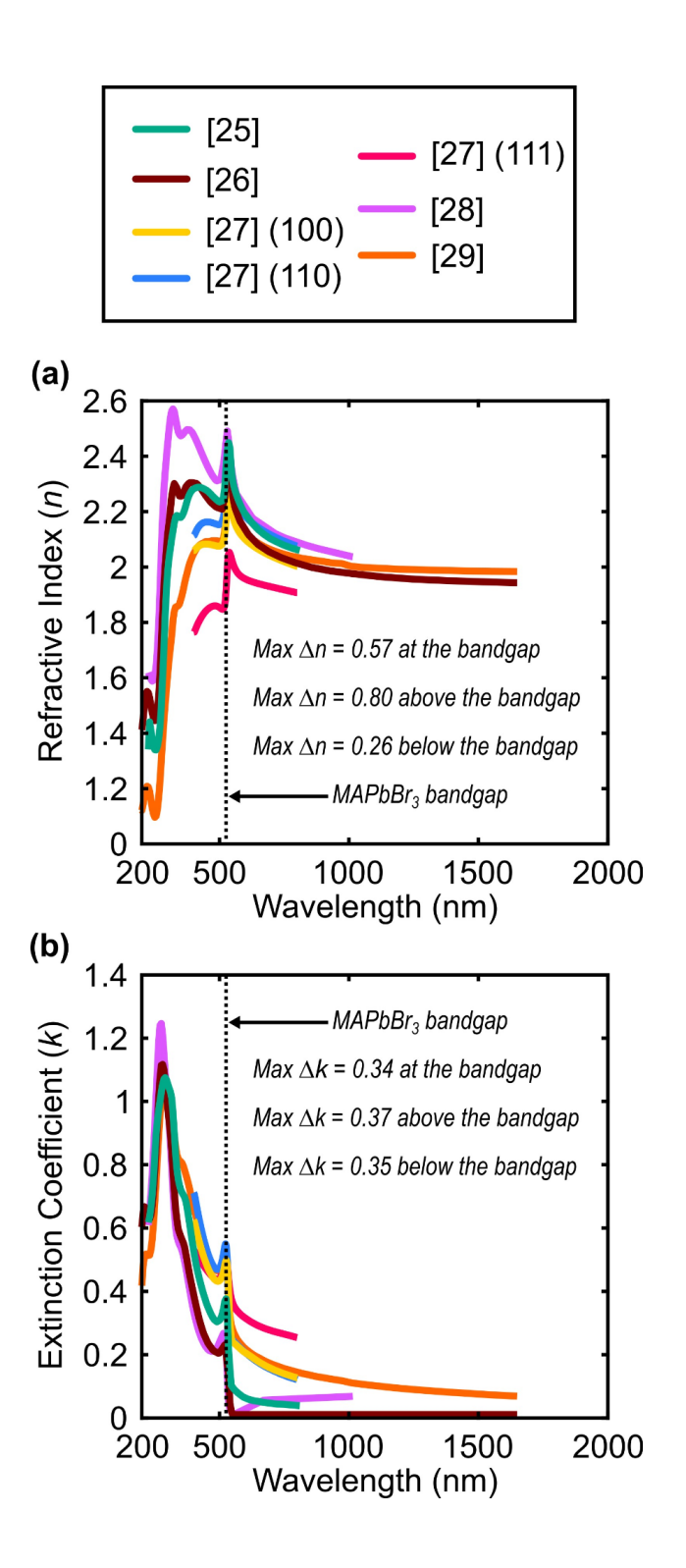


**Figure 2.** Illustrative comparison of representative optical constants for single crystal MAPbBr<sub>3</sub> from the literature (References [25], [26], [27], [28], and [29]), including (a) refractive indices, n, and (b) and extinction coefficients, k.

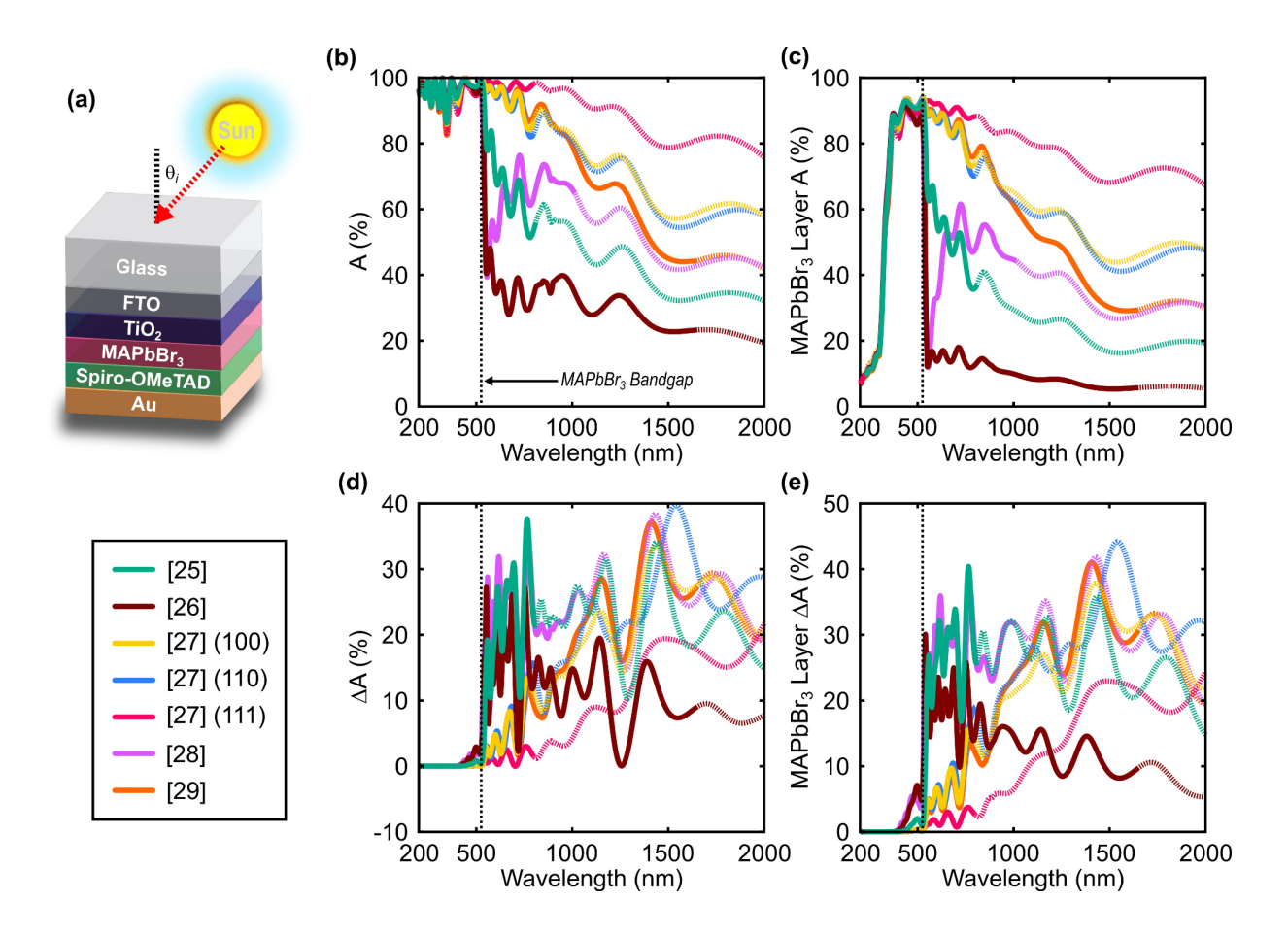


**Figure 3.** Comparison of representative PSC device optical responses using optical constants from Figure 2. Illustration of (a) planar PSC architecture from Ball et al.,<sup>31</sup> (b) unoptimized PSC device absorptance, (c) unoptimized MAPbBr<sub>3</sub> layer absorptance, (d) optimized MAPbBr<sub>3</sub> layer PSC device absorptance defined by Equation 1, and (e) optimized MAPbBr<sub>3</sub> layer change in absorptance defined by Equation 2.

### 3.2. Morphology and Chemical Composition of Single Crystal MAPbBr<sub>3</sub>

In order to establish the high material quality of our single crystal MAPbBr<sub>3</sub>, we turn to a detailed analysis of the crystals surface quality, crystal structure, and chemical composition. Optical profilometry was used to measure the quality of the crystal surface grown at the glass slide interface. **Figure 4a** shows a contour plot of a  $1\times1$  mm<sup>2</sup> area of the crystal surface. The surface roughness (root mean square height,  $S_q$ ) of this area is ~3 nm, indicating that the crystal surface is optically smooth and free of major defects. It is presumed that any defects observed on the crystal surface are imparted from the glass surface that the crystal was grown on. The normalized X-ray diffraction patterns of our MAPbBr<sub>3</sub> crystal match the simulated diffractogram produced from MAPbBr<sub>3</sub> in the Pm<u>3</u>m space group in **Figure 4b**. No impurity peaks are present in the measured diffractogram and the MAPbBr<sub>3</sub> diffraction peaks are indexed to the (100) crystallographic plane and multiples of (100), showing strong preferred orientation of the top crystal surface in the  $\langle 100 \rangle$  crystallographic direction. <sup>32,33</sup>

The MAPbBr<sub>3</sub> surface XPS spectra depict typical surface chemistry characteristics of a sample exposed to ambient atmosphere with an oxygen concentration of about 10.4 at.% and adventitious carbon at about 66 at.%.<sup>34,35</sup> Merged high-resolution XPS spectra of the MAPbBr<sub>3</sub> sample surface, inset table of peak position, integrated peak area, and atomic percentage are shown in **Figure S1**. A survey XPS scan of all measured elements from the surface of the MAPbBr<sub>3</sub> sample is provided in **Figure S2**. The decomposition of the Pb 4*f* spectra (Fig. S3) is modeled by component peaks with binding energy in the range of a native Pb oxide (4 $f_{7/2} \approx 138.4$  and 4 $f_{5/2} \approx 143.3$  eV) and Pb<sup>2+</sup> binding energy of (4 $f_{7/2} \approx 137.6$  and 4 $f_{5/2} \approx 142.6$  eV).<sup>34,36</sup> The O 1*s* core-level peak is modeled (residual STD = 0.582) with four synthetic component peaks (**Figure S3**) with lowest energy component peak having a binding energy comporting with that of Pb oxide at  $\approx 530.6$  eV.<sup>34,36</sup> EDS was also performed to investigate the chemical composition deeper into the

bulk of the crystal (**Figure S4**). The expected 1:3 ratio of Pb:Br was found from EDS (**Table S1**) confirming that only a thin layer of the surface is oxidized while the bulk of the crystal is pure lead halide perovskite.

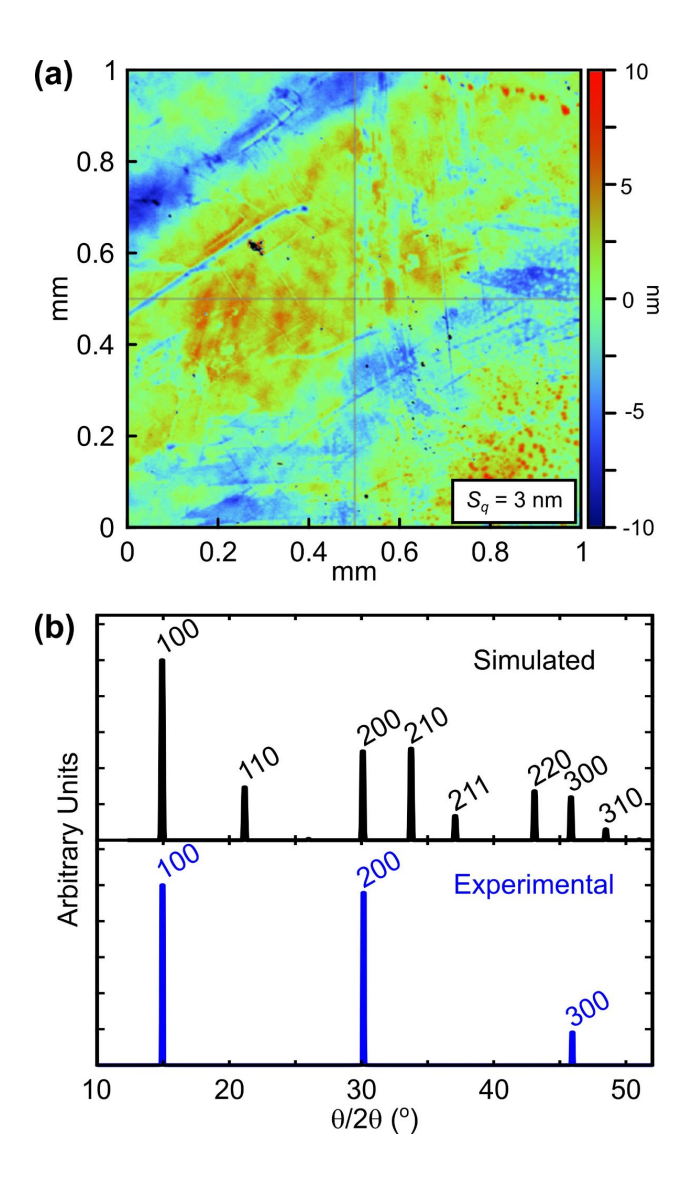


**Figure 4.** Surface roughness and morphology of single crystal MAPbBr<sub>3</sub> grown using a modified ITC method. (a) Image of the optical profilometry scan showing the root mean square height,  $S_q$ ,

of ~3 nm over the 1 mm<sup>2</sup> area. (b) Normalized X-ray diffraction pattern of MAPbBr<sub>3</sub> simulated (top), and the measured (100) crystal plane (bottom).

### 3.3. Optical Dispersion Data Analysis of Single Crystal MAPbBr<sub>3</sub>

Spectroscopic ellipsometry is a useful characterization technique to support the development of high-quality perovskite materials and PSCs. When performing spectroscopic ellipsometry, a known incident polarization state of light interacts with the perovskite sample surface (bulk material) and the reflected (transmitted) light is analyzed to determine the change in amplitude ratio ( $\Psi$ ) and phase ( $\Delta$ ). From this characterization approach, the fundamental optical properties can be derived including the refractive index (n), extinction coefficient (k), dielectric functions ( $\varepsilon_1$  and  $\varepsilon_2$ ), and absorption coefficient ( $\alpha$ ). These interrelated optical properties play a crucial role toward the optimization and resulting efficiency of engineered PSCs. However, inadequate sample preparation, modeling assumptions, and optical dispersion data analysis can lead to an inaccurate derivation of perovskite optical properties (see Section 3.1 and **Figure 2**). As a result, to ensure proper characterization of complex index materials using spectroscopic ellipsometry, it is often necessary to employ more rigorous optical dispersion data analysis methods (discussed here) and quantify associated process-dependent material structure-property relationships (see Section 3.2).

Variable angle spectroscopic ellipsometry was used to measure our MAPbBr<sub>3</sub> single crystal in a wavelength range of 210-2500 nm. These data contain changes to the amplitude ratio ( $\Psi$ , **Figure 5a**) and phase ( $\Delta$ , **Figure 5b**) difference between the p- and s- reflection coefficients of the polarized incident light, but often do not provide necessary sensitivity to low absorption

coefficients of a given material (i.e.,  $\alpha$  <100 cm<sup>-1</sup>).<sup>37</sup> As a result, absorptance characteristics (especially with very fine spectral features observed for MAPbBr<sub>3</sub>) can be under approximated from spectroscopic ellipsometry characterization alone. However, appending spectroscopic ellipsometry data (Figure 5a,b) with transmission intensity data (200-2500 nm, Figure 5c) can provide the necessary optical absorption information to properly derive the optical properties of MAPbBr<sub>3</sub> for both normal and anomalous optical dispersion. Furthermore, in some cases, this appended modeling approach can help improve the accuracy of the analysis and reduce uncertainties in the optical property derivation. As a result, our approach eliminates and/or corrects parameter correlations or insensitivity that could have occurred from optical dispersion data analysis using ellipsometry data alone.<sup>38</sup> It is important to note that our experimentally appended optical analysis essentially yields the effective optical properties of our single crystal MAPbBr<sub>3</sub>, given the subtle oxidation at the surface of the single crystal due to the processing/handling conditions employed (see Figure 4c). A separate oxide layer was assessed in the optical dispersion data analysis for comparison, but resulted in negligible influence (i.e., little change to the mean squared error, MSE, of the fits) to the derived optical properties. As such, an oxide layer was not included here for simplicity of illustration. However, the influence of the oxide layer is captured in our experimentally appended optical dispersion data analysis (i.e., the impact on optical transmission is captured). Given the minimal surface oxidation, we consider these effective optical properties a close approximation of fully stoichiometric MAPbBr<sub>3</sub>.

This appended modeling approach is necessary for MAPbBr<sub>3</sub> to improve anomalous optical dispersion sensitivity to the bandgap transition regime as well as lower-order spectral overtones. Here, spectral overtones refer to the presence of other optically absorbing species in the perovskite material. While some have suggested perovskites are nearly transparent in the infrared regime<sup>15</sup>

this is not the case for hybrid organic-inorganic perovskites. Although not phenomenologically quantified with respect to material species and optical absorption mechanics, in the case of MAPbBr<sub>3</sub>, the MA moieties represent compositional species that contribute to the optical absorptance peaks below the band edge. For example, we observe spectral overtone features beginning at ~1050 nm that continue to longer wavelengths shown in the transmission intensity spectra in **Figure 5c**. To generate a robust derivation of MAPbBr<sub>3</sub> optical properties, it is necessary to include these anomalous optical dispersion characteristics at, above, and below the bandgap in the optical dispersion data analysis. To our knowledge, no complementary modeling methodology has been reported for MAPbX<sub>3</sub>;<sup>15</sup> however, this characterization approach has been demonstrated for other complex index thin films with anomalous optical dispersion.<sup>38,39</sup> In part, the lack of such complementary analysis for MAPbBr<sub>3</sub> to date may be due to limited single crystal material/surface quality and sample size dimensions necessary to generate low scattering transmission intensity spectra.

We use a Kramers-Kronig consistent basis-spline (B-spline) model to facilitate our appended optical dispersion data analysis. 40,41 The B-spline function is a piecewise polynomial function that consists of multiple segments, each of which is defined by a set of control points and the polynomial degree. This analysis method results in a smooth and continuous function across the modeled segments, which can then be adjusted to fit the experimental data using conventional optimization algorithms. The B-spline formalism was used here to fit both the experimental spectroscopic ellipsometry and transmission data (**Figure 5a-c**). The modeled results in **Figure 5** show reasonable profile fits of the fine spectral features above and below the bandgap for MAPbBr<sub>3</sub>. By comparison, fitting fine spectral features is not easily done using a conventional general oscillator model approach (e.g., Gaussian, Lorentz, Tauc-Lorentz, Cody-Lorentz, or

Tanguy formalisms). Our spectroscopic ellipsometry and transmission intensity appended modeling approach with a Kramers-Kronig consistent high resolution B-spline fit yields a rigorous optical dispersion data analysis of single crystal MAPbBr<sub>3</sub>.

The optical properties derived from our analysis are shown in **Figure 5d**. These optical dispersion curves provide well-approximated spectral characteristics at, above, and below the bandgap for MAPbBr<sub>3</sub>. At the scales shown in **Figure 5d**, the influence of the MA overtones below the bandgap are not depicted well. **Figure 5e** shows a logarithmic y-axis scale for k, which shows the fine features of the MA overtone anomalous optical dispersion. These data illustrate another advantage of employing spectroscopic ellipsometry and transmission intensity data appended optical dispersion analysis. Reflection mode spectroscopic ellipsometry alone typically does not offer sufficient sensitivity for the derived optical constants below  $\sim 10^{-3}$ . However, by including transmission intensity data in the analysis, we improve optical property derivation sensitivity to below  $10^{-5}$  (or commensurate with the sensitivity of the spectrophotometer detector) specifically for the extinction coefficient because of the long path length through the sample. The dielectric functions and absorption coefficients for our single crystal MAPbBr<sub>3</sub> are shown in **Figure S5**. Tabulated data for the optical constants, dielectric functions, and absorption coefficients are provided in the Supplementary Information CSV data file.

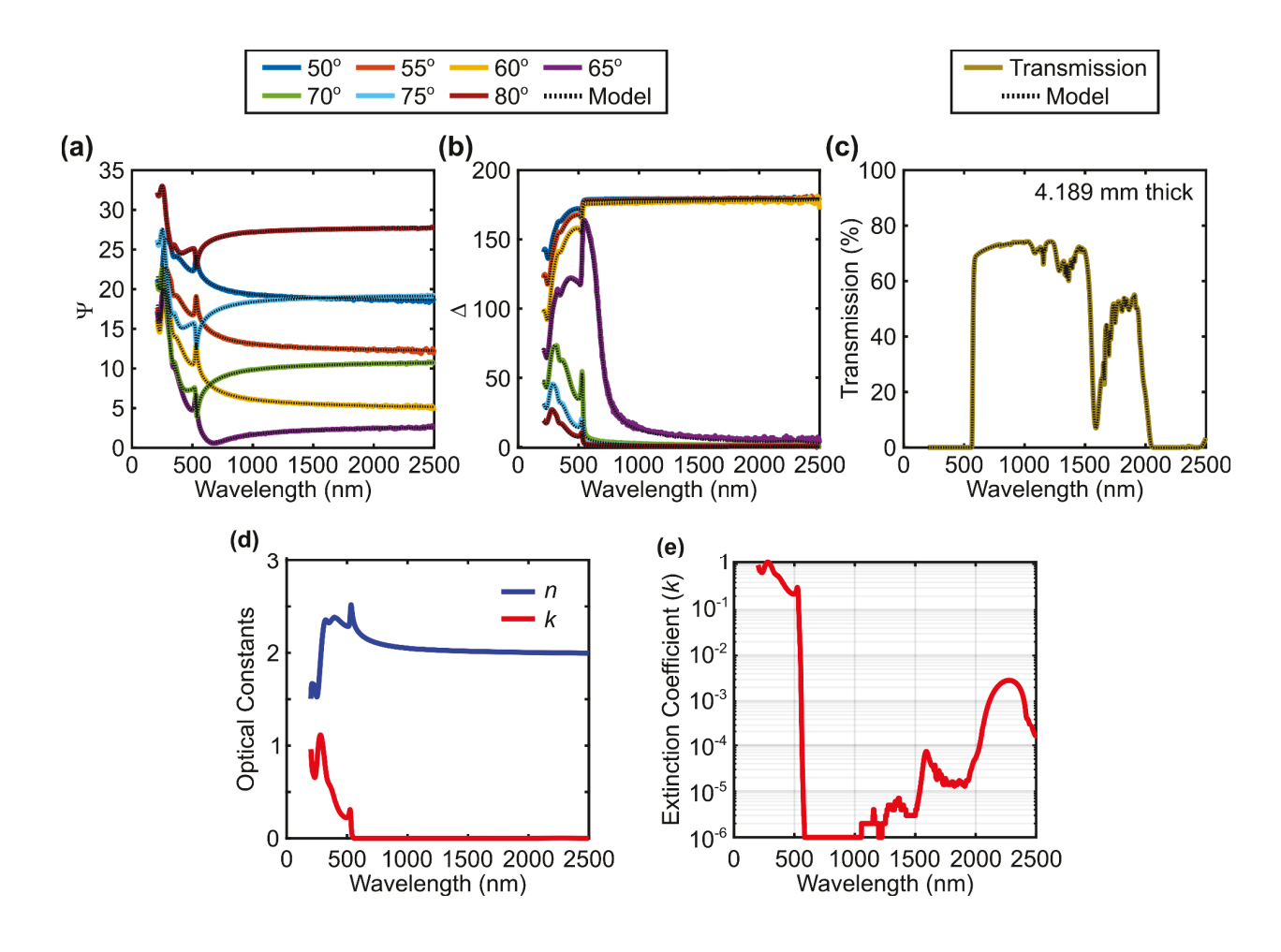


**Figure 5.** Optical dispersion data analysis and the derived optical constants of single crystal MAPbBr<sub>3</sub> grown using a modified ITC method. Reflectance ellipsometry data for (a)  $\Psi$  and (b)  $\Delta$  with associated modeled fits at angles 50-80°. (c) Transmission intensity data with the associated modeled fit at normal incidence with a MAPbBr<sub>3</sub> thickness of 4.189 mm. (d) The refractive index, n, and extinction coefficient, k, derived using the fits shown in a-c. (e) Extinction coefficient, k, with a logarithmic y-axis scale to show the sharp band edge transition and MA overtones captured using our experimentally appended optical dispersion data analysis method.

### 3.4. Active Layer Absorptance Optimization of Illustrative MAPbBr<sub>3</sub> PSCs

Representative PSC designs were modeled using the derived data shown in **Figure 5d,e** for MAPbBr<sub>3</sub> with the device architecture shown in **Figure 3a**. These designs are compared in **Table 1** representing three different examples for illustration: PSC Design I with no optimization in the design with layer thicknesses fixed as reported by Ball et al.,<sup>31</sup> PSC Design II with the MAPbBr<sub>3</sub> absorbing layer optimized (all other layers fixed in thickness as in PSC Design I), and PSC Design III with the MAPbBr<sub>3</sub>, FTO, and Au layers optimized for MAPbBr<sub>3</sub> layer absorptance (all other layers fixed in thickness as in PSC Design I).

The modeled optical responses for these designs are shown in **Figure 6**. Spectra include the total optical reflection (R), transmission (T), and absorptance (A) for the illustrative PSC device (**Figure 3a**) involving impinging light at normal incidence (or the angle of incidence, AOI, = 0°) shown in **Figure 6a-c** for the different designs. **Figure 6a** shows the responses for PSC Design I. Here, we observe improvements in the modeled responses due to the use of our derived optical constants (**Figure 5**) as compared to illustrative literature responses shown in **Figure 3b** (i.e., using the optical constants shown in **Figure 2** in the PSC design configuration). PSC Design I shows a very sharp transition at the MAPbBr<sub>3</sub> bandgap (~539 nm) and low parasitic optical absorptance below the bandgap in comparison to illustrative design examples shown in **Figure 3b**.

Figure 6b shows the response for PSC Design II where the MAPbBr<sub>3</sub> layer was optimized for optical absorptance (all other layers fixed in thickness). There is a small improvement in total absorptance for PSC Design II compared to PSC Design I. However, PSC Design III shows a more distinct change in total optical absorptance characteristics compared to PSC Design I and II. PSC Design III includes more layer optimization as compared to the other designs, which, subsequently, results in a greater impact toward maximizing MAPbBr<sub>3</sub> layer absorptance while minimizing parasitic absorptance of light at, above, and below the MAPbBr<sub>3</sub> band edge. It is important to note

that the optical responses shown in **Figure 6a-c** represent the desired MAPbBr<sub>3</sub> layer absorptance as well as undesired parasitic optical absorptance as a result of the device design.

The impact of each respective layer optimization is further depicted in **Figure 6d-f** illustrating individual layer absorptance (A) in the given PSC device design. Any optical absorptance by material layers in the device other than MAPbBr<sub>3</sub> represents undesired parasitic absorptance. PSC Design I shows the baseline response with respect to the non-optimized device design (**Figure 6d**). Here, the MAPbBr<sub>3</sub> layer exhibits the greatest peak absorptance above 539 nm followed by FTO and Au. MAPbBr<sub>3</sub> exhibits the lowest absorptance below 539 nm; however, there is parasitic absorptance from all other layers at these wavelengths. PSC Design II layer absorptance yields very similar results to PSC Design I, except there is a small peak increase in the MAPbBr<sub>3</sub> layer absorptance for Design II below 539 nm. Despite optimizing for MAPbBr<sub>3</sub> layer absorptance in the device, the minimal increase in absorptance is due to the fixed thicknesses for all other layers in the design. This is primarily due to the FTO layer exhibiting greater parasitic absorptance above and below the bandgap, with Au contributing next to the most parasitic absorptance below the MAPbBr<sub>3</sub> bandgap.

To further maximize MAPbBr<sub>3</sub> layer absorptance and minimize parasitic absorptance by non-active layers in the PSC device, we optimize MAPbBr<sub>3</sub> layer absorptance while permitting changes to FTO and Au layer thicknesses. The impact of permitting the parameterization of just these three layers in the device is shown in **Figure 6f**. Here, a noticeable increase in peak MAPbBr<sub>3</sub> absorptance below the bandgap is observed along with a considerable decrease in parasitic absorptance across all wavelengths above 400 nm (the arbitrarily selected target wavelength cutoff of the MAPbBr<sub>3</sub> optimization for the PSC design). We evaluated the performance of the PSC device with parameterization of all layer thicknesses; however, little improvement was observed

between PSC Design III and an all-layer thickness parameterization design (not shown). Overall, PSC Design III suggests it is possible to carry out PSC design iterations constrained by physical thickness limits of the non-active layers, for instance, in order to maintain electronic performance of the contact and electron/hole transport layers while optimizing overall optical performance.

The optical performance of a given PSC in practice also includes the angle of the incident of light, which will be strongly influenced by the design. **Figure 6g-i** show the total absorptance for the respective PSC designs from 0-90° AOI as a function of wavelength, where 0° represents the incident light normal to the device interface. PSC Designs I and II show very similar AOI performance with a noticeable increase in parasitic absorptance below the band edge at ~50° AOI. This increase in parasitic optical absorptance originates as a result of each individual layer material optical properties and is a direct artifact of the PSC device design (layer thicknesses of the non-active layers within the PSC). PSC Design III in **Figure 6i** shows no such spectral artifact at ~50° AOI and an improvement in device optical absorptance at and below the MAPbBr<sub>3</sub> bandgap as a function of AOI, which further demonstrates the need to optimize the optical performance of selected material layers in a given PSC. By selectively expanding the design optimization, Design III shows that the MAPbBr<sub>3</sub> layer absorptance can be strategically improved, parasitic absorptance by the other device layers can be decreased at all wavelengths, and total device optical performance can be refined up to high angles of incidence.

Overall, these modeled PSC designs demonstrate the critical influence of accurate optical property determination in order to further improve the optical performance of modeled PSC devices. Most influential for these illustrative planar thin film device designs is capturing MAPbBr<sub>3</sub> optical behavior at the band edge transition and below. Also present in each of these designs (**Table 1** and **Figure 6**) is the influence of the MA overtones of MAPbBr<sub>3</sub>. It is also

important to note that the influence of these spectral features at the reported layer thicknesses (Table 1) are subtle but not negligible, and these can impact optical performance below the bandgap. Such material optical characteristics have the potential to yield unexpected optical or device behavior if unaccounted for in the given PSC optical coating design (i.e., R, T, and A including the performance at different angles of incidence). The impact of such features will become more significant with increased MAPbBr<sub>3</sub> layer thicknesses due to an increase in solar radiation attenuation.

Table 1. Description and layer thicknesses in nanometers for each MAPbBr<sub>3</sub> PSC design illustration.

	PSC Design I	PSC Design II	PSC Design III
Design Description	No layer optimization	MAPbBr <sub>3</sub> layer absorptance optimization	MAPbBr <sub>3</sub> layer absorptance + FTO + Au optimization
FTO	420	420	33
TiO <sub>2</sub>	41	41	41
MAPbBr <sub>3</sub>	492	1228	1082
Spiro-OMeTAD	253	253	253
Au	30	30	303

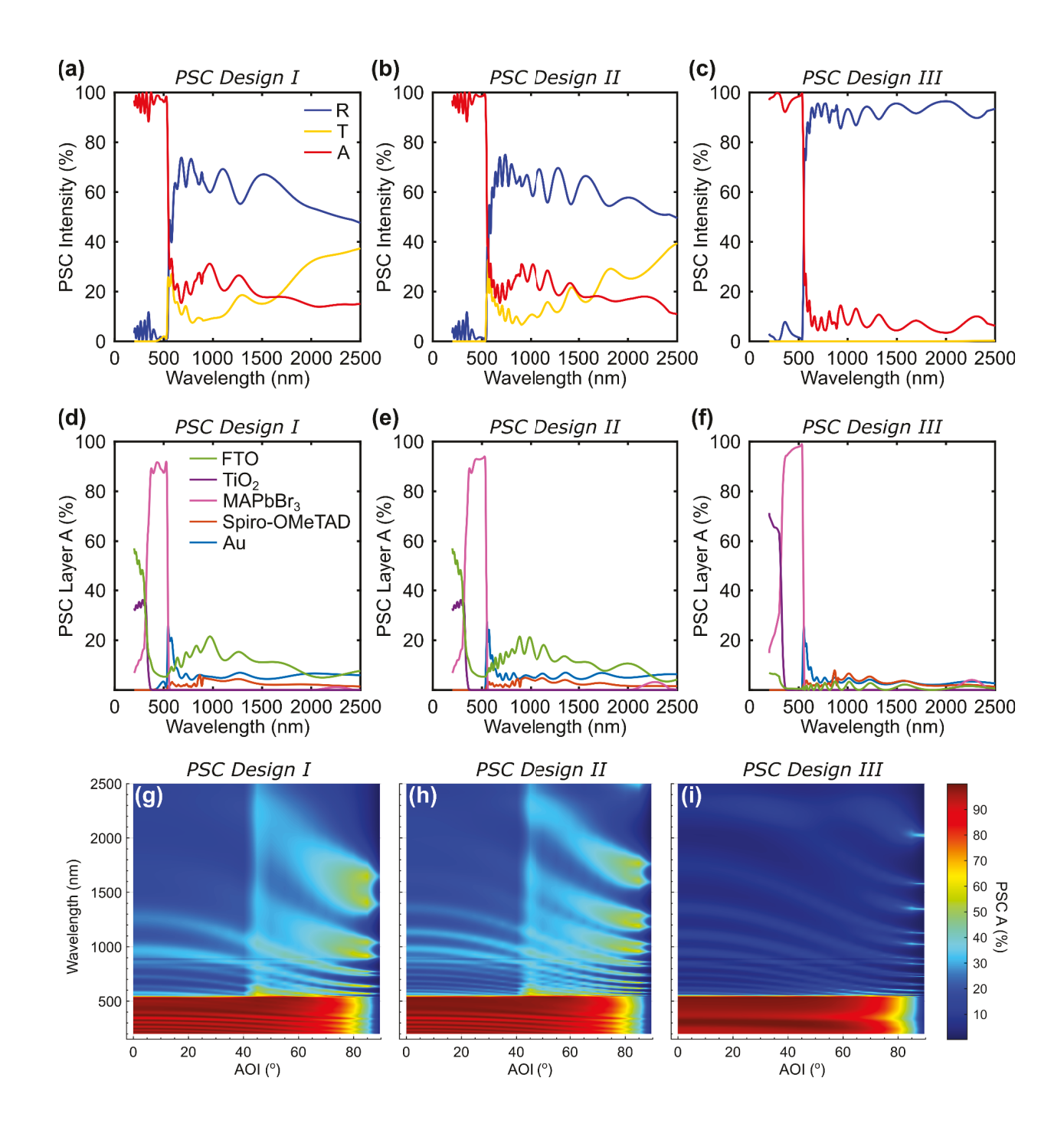


**Figure 6.** Comparison of modeled PSC Design I, II, and III spectral performance. (a-c) Comparison of R%, T%, and A% spectra for each design at normal incidence. (d-f) Comparison of each PSC layer A% for reach design at normal incidence. (g-i) PSC A% as a function of wavelength vs. AOI (0-90°).

### 4. CONCLUSIONS

In this work, using high optical quality single crystal MAPbBr<sub>3</sub> from a modified ITC growth process, we derived MAPbBr<sub>3</sub> optical constants using a rigorous optical dispersion data analysis method involving variable angle spectroscopic ellipsometry data appended with transmission intensity data. Our analysis resulted in a robust fit of the fine MAPbBr<sub>3</sub> optical characteristics including the bandgap transition at ~539 nm and the MA overtone features in the infrared regime. The accurate derivation of these spectral features enabled realistic modeling of optical performance involving a representative modeled MAPbBr<sub>3</sub> PSC device. Our optical dispersion data analysis used to derive the optical properties of MAPbBr<sub>3</sub> is applicable to all perovskite analogs. As such, careful optical property determination is expected to further enhance the modeling, simulation, and device development of targeted optoelectronic and photovoltaic perovskite devices. The modeled optical performance in this work focused on UV to infrared wavelengths with behavior at, above, and below the bandgap of the active perovskite layer material for a single junction planar solar cell. The development of planar or structured multijunction PSCs and hybrid active layer perovskite-based solar cells that perform across a broader solar absorption spectrum are in development and expected to further compete with state of the art highperformance silicon solar cells. All such devices will inevitably depend on the robust derivation of active and non-active layer material optical constants to ensure realistically modeled device performance under associated process-induced device fabrication constraints.

### ASSOCIATED CONTENT

The Supporting Information is available free of charge (URL).

Merged high-resolution XPS spectra, survey XPS spectra, high-resolution core level spectra and

peak fits, EDS spectrum, and elemental composition of the MAPbBr<sub>3</sub> single crystal. (PDF)

**AUTHOR INFORMATION** 

**Corresponding Author** 

\*Email: christopher.mccleese.1.ctr@us.af.mil

\*Email: peter.stevenson.2@us.af.mil

Notes

The authors declare no competing financial interest.

**ACKNOWLEDGMENTS** 

This work was supported by the Materials and Manufacturing Directorate within the U.S. Air

Force Research Laboratory (AFRL) via contract numbers FA8650-16-5404-0016 and FA8650-22-

D-5408. M.C.B. and T.A.G. acknowledge the support from the Air Force Office of Scientific

Research grant number 23RXCOR023. N.E. and C.V.R. acknowledge support from the National

Science Foundation (NSF) with NSF-PREM grant (DMR-1827745) and the NSF-AFRL INTERN

Program (DCL NSF 21-029).

31

### **REFERENCES**

- (1) Jung, H. S.; Park, N.-G. Perovskite Solar Cells: From Materials to Devices. *Small* **2015**, *11* (1), 10–25.
- (2) Ahmadi, M.; Wu, T.; Hu, B. A Review on Organic-Inorganic Halide Perovskite Photodetectors: Device Engineering and Fundamental Physics. *Adv. Mater.* **2017**, *29* (41). https://doi.org/10.1002/adma.201605242.
- (3) Fu, Y.; Zhu, H.; Chen, J.; Hautzinger, M. P.; Zhu, X.-Y.; Jin, S. Metal Halide Perovskite Nanostructures for Optoelectronic Applications and the Study of Physical Properties. *Nature Reviews Materials* **2019**, *4* (3), 169–188.
- (4) Shellaiah, M.; Sun, K. W. Review on Sensing Applications of Perovskite Nanomaterials.

  Chemosensors 2020, 8 (3), 55.
- (5) Sun, C.; Alonso, J. A.; Bian, J. Recent Advances in Perovskite-type Oxides for Energy Conversion and Storage Applications. *Adv. Energy Mater.* **2021**, *11* (2), 2000459.
- (6) Feng, A.; Xie, S.; Fu, X.; Chen, Z.; Zhu, W. Inch-Sized Thin Metal Halide Perovskite Single-Crystal Wafers for Sensitive X-Ray Detection. Front Chem 2021, 9, 823868.
- (7) Kundu, S.; O'Connell, J.; Hart, A.; Richtsmeier, D.; Bazalova-Carter, M.; Saidaminov, M. I. Halide Perovskites for Direct Conversion Megavoltage X-ray Detectors. *Adv. Electron. Mater.* 2022, 8 (12), 2200640.
- (8) Cui, F.; Zhang, P.; Zhang, L.; Hua, Y.; Sun, X.; Li, X.; Zhang, G.; Tao, X. Liquid-Phase Epitaxial Growth of Large-Area MAPbBr<sub>3-n</sub>cl<sub>n</sub>/CsPbBr<sub>3</sub> Perovskite Single-Crystal Heterojunction for Enhancing Sensitivity and Stability of X-Ray Detector. *Chem. Mater.* **2022**. https://doi.org/10.1021/acs.chemmater.2c02266.
- (9) Koh, T. M.; Thirumal, K.; Soo, H. S.; Mathews, N. Multidimensional Perovskites: A Mixed

- Cation Approach Towards Ambient Stable and Tunable Perovskite Photovoltaics. *ChemSusChem* **2016**, *9* (18), 2541–2558.
- (10) Asghar, M. I.; Zhang, J.; Wang, H.; Lund, P. D. Device Stability of Perovskite Solar Cells A Review. *Renewable Sustainable Energy Rev.* **2017**, *77*, 131–146.
- (11) Rong, Y.; Hu, Y.; Mei, A.; Tan, H.; Saidaminov, M. I.; Seok, S. I.; McGehee, M. D.; Sargent, E. H.; Han, H. Challenges for Commercializing Perovskite Solar Cells. *Science* 2018, 361 (6408). https://doi.org/10.1126/science.aat8235.
- (12) Boyd, C. C.; Cheacharoen, R.; Leijtens, T.; McGehee, M. D. Understanding Degradation Mechanisms and Improving Stability of Perovskite Photovoltaics. *Chem. Rev.* **2019**, *119* (5), 3418–3451.
- (13) Green, M. A.; Ho-Baillie, A.; Snaith, H. J. The Emergence of Perovskite Solar Cells. *Nat. Photonics* **2014**, *8* (7), 506–514.
- (14) Ansari, M. I. H.; Qurashi, A.; Nazeeruddin, M. K. Frontiers, Opportunities, and Challenges in Perovskite Solar Cells: A Critical Review. *J. Photochem. Photobiol. C: Photochem. Rev.* 2018, 35, 1–24.
- (15) Li, H.; Cui, C.; Xu, X.; Bian, S.; Ngaojampa, C.; Ruankham, P.; Jaroenjittchai, A. P. A Review of Characterization of Perovskite Film in Solar Cells by Spectroscopic Ellipsometry. Solar Energy 2020, 212, 48–61.
- (16) Tailor, N. K.; Abdi-Jalebi, M.; Gupta, V.; Hu, H.; Ibrahim Dar, M.; Li, G.; Satapathi, S. Recent Progress in Morphology Optimization in Perovskite Solar Cell. J. Mater. Chem. A Mater. Energy Sustain. 2020, 8 (41), 21356–21386.
- (17) Lee, Y.; Park, C.; Balaji, N.; Lee, Y.-J.; Dao, V. A. High-Efficiency Silicon Solar Cells: A Review. Isr. J. Chem. 2015, 55 (10), 1050–1063.

- (18) Andreani, L. C.; Bozzola, A.; Kowalczewski, P.; Liscidini, M.; Redorici, L. Silicon Solar Cells: Toward the Efficiency Limits. *Advances in Physics: X* **2019**, *4* (1), 1548305.
- (19) Yang, W.; Yang, Z.; Shou, C.; Sheng, J.; Yan, B.; Ye, J. Optical Design and Optimization for Back-Contact Perovskite Solar Cells. *Solar Energy* **2020**, *201*, 84–91.
- (20) Deng, K.; Li, L. Optical Design in Perovskite Solar Cells. *Small Methods* **2020**, *4* (6), 1900150.
- (21) Rani, S.; Kumar, A.; Ghosh, D. S. Optical Designing of Perovskite Solar Cells. *IEEE Journal of Photovoltaics* **2022**, *12* (2), 595–601.
- (22) Matson, R. J.; Emery, K. A.; Bird, R. E. Terrestrial Solar Spectra, Solar Simulation and Solar Cell Short-Circuit Current Calibration: A Review. *Solar Cells* **1984**, *11* (2), 105–145.
- (23) Liu, Y.; Zhang, Y.; Yang, Z.; Feng, J.; Xu, Z.; Li, Q.; Hu, M.; Ye, H.; Zhang, X.; Liu, M.; Zhao, K.; Liu, S. Low-Temperature-Gradient Crystallization for Multi-Inch High-Quality Perovskite Single Crystals for Record Performance Photodetectors. *Mater. Today* 2019, 22, 67–75.
- (24) Fairely, N. CasaXPS Manual 2.3. 15. Casa Software Ltd 2009.
- (25) Mannino, G.; Deretzis, I.; Smecca, E.; Giannazzo, F.; Valastro, S.; Fisicaro, G.; La Magna, A.; Ceratti, D.; Alberti, A. CsPbBr3, MAPbBr3, and FAPbBr3 Bromide Perovskite Single Crystals: Interband Critical Points under Dry N2 and Optical Degradation under Humid Air. *J. Phys. Chem. C* 2021, 125 (9), 4938–4945.
- (26) Park, J.-S.; Choi, S.; Yan, Y.; Yang, Y.; Luther, J. M.; Wei, S.-H.; Parilla, P.; Zhu, K. Electronic Structure and Optical Properties of α-CH3NH3PbBr3 Perovskite Single Crystal. J. Phys. Chem. Lett. 2015, 6 (21), 4304–4308.
- (27) Zhang, L.; Cui, S.; Guo, Q.; Ge, C.; Han, Q.; Lin, Q.; Li, C.; Zheng, X.; Zhai, Z.; Wang, L.;

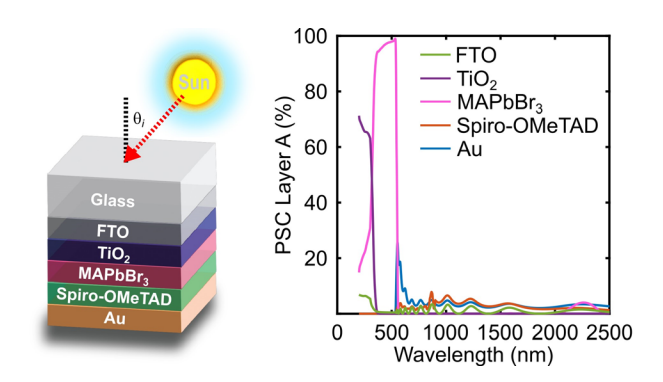
- Sun, Q.; Xu, Y.; Liu, Y.; Tao, X. Anisotropic Performance of High-Quality MAPbBr3 Single-Crystal Wafers. *ACS Appl. Mater. Interfaces* **2020**, *12* (46), 51616–51627.
- (28) Leguy, A. M. A.; Azarhoosh, P.; Alonso, M. I.; Campoy-Quiles, M.; Weber, O. J.; Yao, J.; Bryant, D.; Weller, M. T.; Nelson, J.; Walsh, A.; van Schilfgaarde, M.; Barnes, P. R. F. Experimental and Theoretical Optical Properties of Methylammonium Lead Halide Perovskites. *Nanoscale* **2016**, *8* (12), 6317–6327.
- (29) Laysandra, H.; Chao, Y.-C.; Liu, H.-L. Assessing Optical Properties of CH3NH3PbBr3 Single Crystals across the Structural Phase Transitions by Spectroscopic Ellipsometry. *J. Phys. Chem. C* **2022**, *126* (1), 797–805.
- (30) Steger, M.; Janke, S. M.; Sercel, P. C.; Larson, B. W.; Lu, H.; Qin, X.; Yu, V. W.-Z.; Blum, V.; Blackburn, J. L. On the Optical Anisotropy in 2D Metal-Halide Perovskites. *Nanoscale* **2022**, *14* (3), 752–765.
- (31) Ball, J. M.; Stranks, S. D.; Hörantner, M. T.; Hüttner, S.; Zhang, W.; Crossland, E. J. W.; Ramirez, I.; Riede, M.; Johnston, M. B.; Friend, R. H.; Snaith, H. J. Optical Properties and Limiting Photocurrent of Thin-Film Perovskite Solar Cells. *Energy Environ. Sci.* **2015**, *8* (2), 602–609.
- (32) López, C. A.; Martínez-Huerta, M. V.; Alvarez-Galván, M. C.; Kayser, P.; Gant, P.; Castellanos-Gomez, A.; Fernández-Díaz, M. T.; Fauth, F.; Alonso, J. A. Elucidating the Methylammonium (MA) Conformation in MAPbBr3 Perovskite with Application in Solar Cells. *Inorg. Chem.* 2017, 56 (22), 14214–14219.
- (33) Liang, A.; Gonzalez-Platas, J.; Turnbull, R.; Popescu, C.; Fernandez-Guillen, I.; Abargues, R.; Boix, P. P.; Shi, L.-T.; Errandonea, D. Reassigning the Pressure-Induced Phase Transitions of Methylammonium Lead Bromide Perovskite. *J. Am. Chem. Soc.* **2022**, *144*

- (43), 20099–20108.
- (34) Vincent Crist, B. *Handbook of Monochromatic XPS Spectra: The Elements of Native Oxides*; John Wiley & Sons, 2000.
- (35) Crist, B. V. The XPS Library Website: A Resource for the XPS Community Including The XPS Library of Information, XPS Spectra-Base Having >70,000 Monochromatic XPS Spectra, and Spectral Data Processor (SDP) v8.0 Software. *J. Electron Spectros. Relat. Phenomena* **2021**, 248 (147046), 147046.
- (36) Powell, C. J.; Jablonski, A.; Naumkin, A.; Kraut-Vass, A.; Conny, J. M.; Rumble, J. R., Jr. NIST Data Resources for Surface Analysis by X-Ray Photoelectron Spectroscopy and Auger Electron Spectroscopy. J. Electron Spectros. Relat. Phenomena 2001, 114-116, 1097–1102.
- (37) Fujiwara, H. Spectroscopic Ellipsometry: Principles and Applications; John Wiley & Sons, 2007.
- (38) Hilfiker, J. N.; Singh, N.; Tiwald, T.; Convey, D.; Smith, S. M.; Baker, J. H.; Tompkins, H.
   G. Survey of Methods to Characterize Thin Absorbing Films with Spectroscopic Ellipsometry. *Thin Solid Films* 2008, 516 (22), 7979–7989.
- (39) Sun, L.; Grant, J. T.; Jones, J. G.; Murphy, N. R.; Vernon, J. P.; Stevenson, P. R. Tailoring the Optical Properties of Nanoscale-Thick Metal–Dielectric Ag–SiO2 Nanocomposite Films for Precision Optical Coating Integration. *ACS Appl. Nano Mater.* **2023**, *6* (9), 7704–7714.
- (40) Hilfiker, J. N.; Tiwald, T. Dielectric Function Modeling. In Spectroscopic Ellipsometry for Photovoltaics: Volume 1: Fundamental Principles and Solar Cell Characterization; Fujiwara, H., Collins, R. W., Eds.; Springer International Publishing: Cham, 2018; pp 115– 153.
- (41) Likhachev, D. V. Certain Topics in Ellipsometric Data Modeling with Splines: A Review of

Recent Developments. Advanced Optical Technologies 2022, 11 (3-4), 93-115.

(42) Tompkins, H.; Irene, E. A. Handbook of Ellipsometry; William Andrew, 2005.

## For Table of Contents Only



# **Supporting Information**

# Optical Dispersion Data Analysis of Single Crystal MAPbBr<sub>3</sub> for Optimized Perovskite Solar Cell Active Layer Absorptance

Christopher L. McCleese, <sup>1,2,\*</sup> Michael C. Brennan, <sup>1,3</sup> Nathan Episcopo, <sup>4</sup> Lirong Sun, <sup>1,3</sup> Nina Hong, <sup>5</sup> C. V. Ramana, <sup>4,6</sup> Tod A. Grusenmeyer<sup>1,\*</sup>, and Peter R. Stevenson, <sup>1,\*</sup>

<sup>1</sup>Materials and Manufacturing Directorate, Air Force Research Laboratory, Wright-Patterson Air Force Base, Ohio, 45433, USA

<sup>2</sup>General Dynamics Information Technology, 5000 Springfield St. Suite 200, Dayton, Ohio, 45431, USA

<sup>3</sup>Azimuth Corporation, 2970 Presidential Drive, #200, Fairborn, Ohio, 45324, USA

<sup>4</sup>Center for Advanced Materials Research, University of Texas at El Paso, 500 W. University Ave., El Paso, Texas 79968, USA

<sup>5</sup>J.A. Woollam Company, 311 South 7th St. Lincoln, Nebraska, 68508, USA

<sup>6</sup>Department of Aerospace & Mechanical Engineering, University of Texas at El Paso, 500 W.

University Ave., El Paso, Texas 79968, USA

\*Email: christopher.mccleese.1.ctr@us.af.mil

\*Email: peter.stevenson.2@us.af.mil

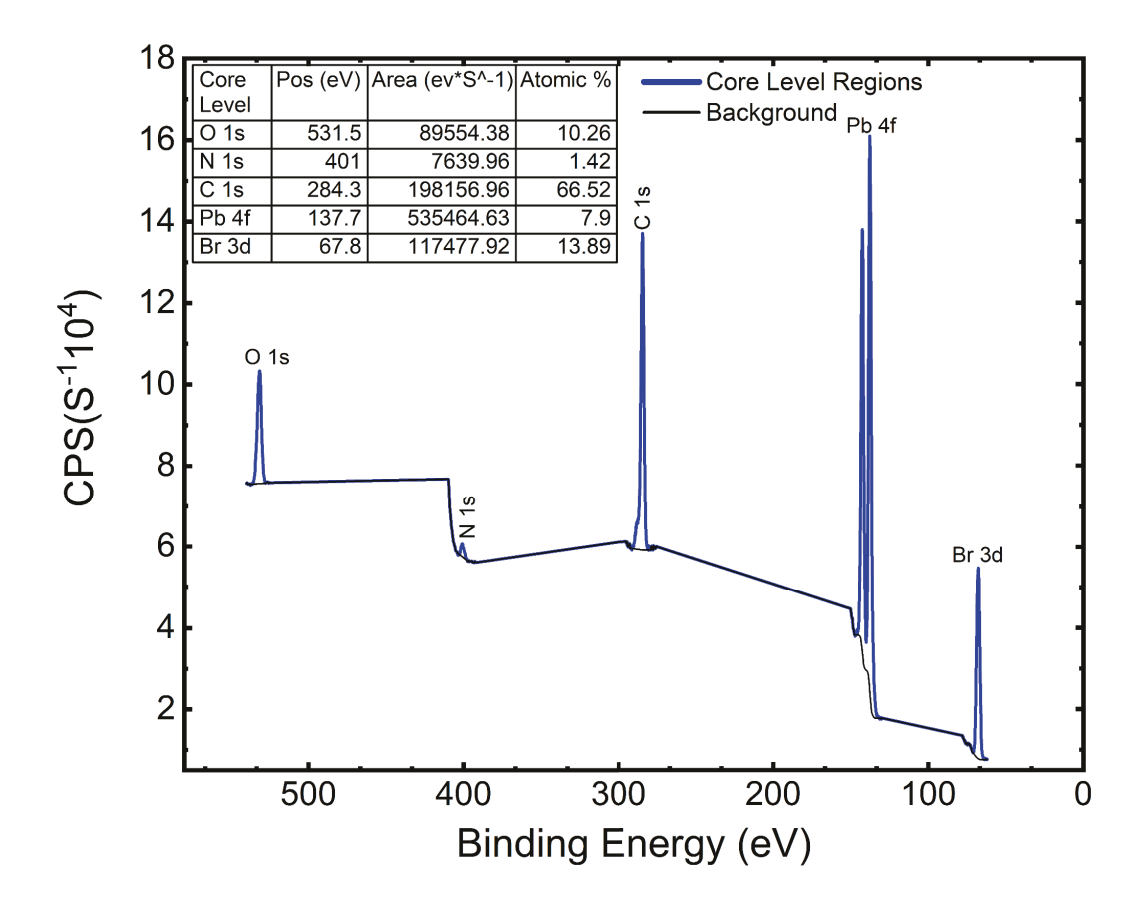


**Figure S1.** Merged high-resolution XPS spectra of the MAPbBr<sub>3</sub> sample surface, inset table of peak position, integrated peak area, and atomic percentage.

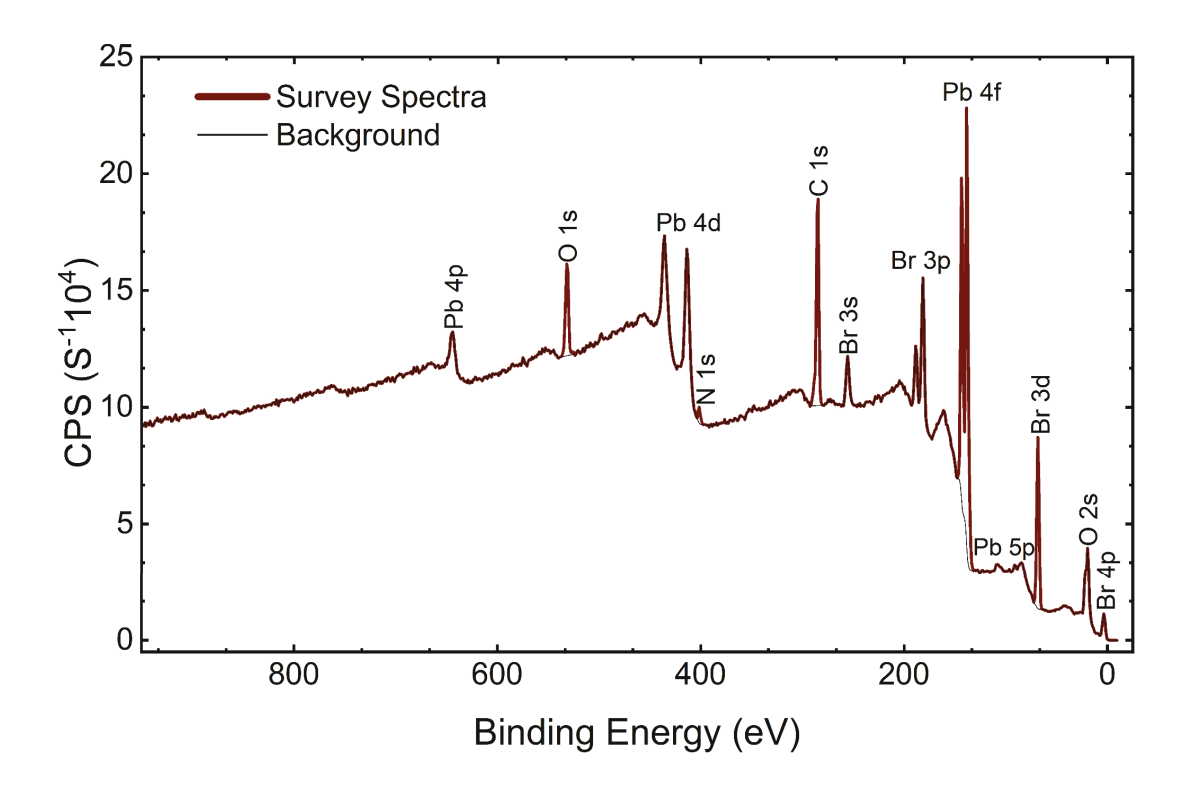
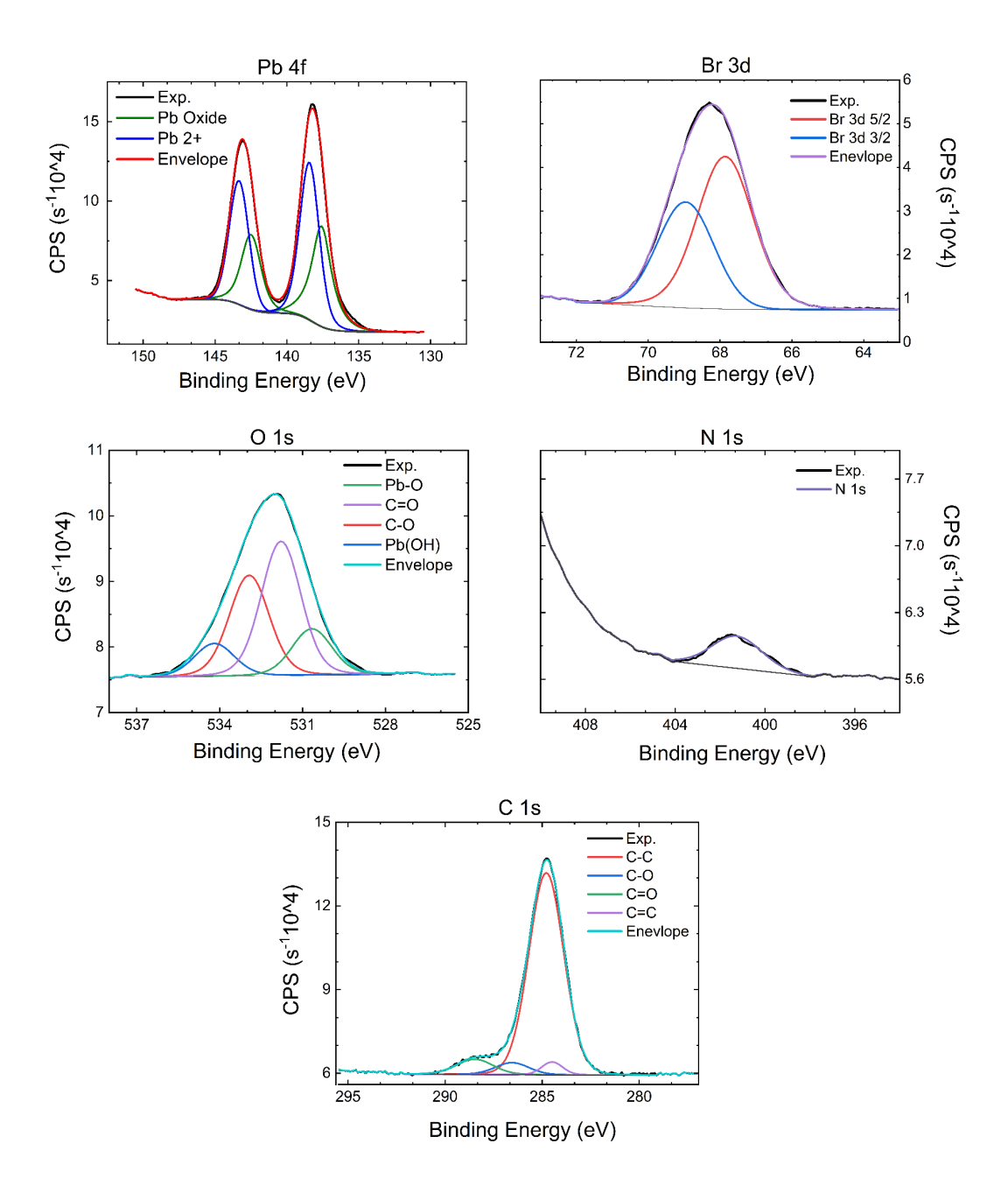
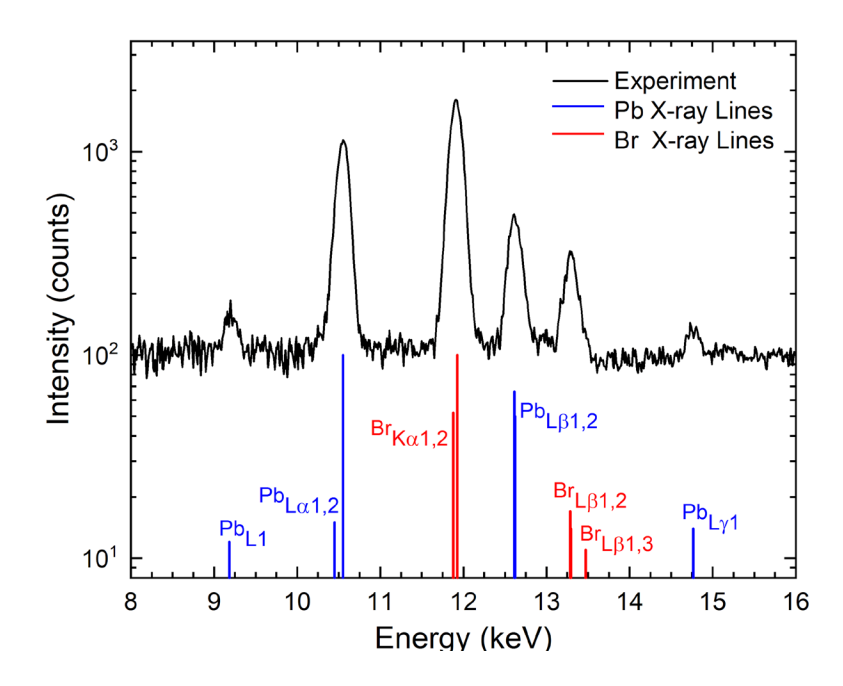


Figure S2. Survey XPS scan of all measured elements from the surface of the MAPbBr3 sample.



**Figure S3.** High-resolution core level spectra for all elements measured on the MAPbBr<sub>3</sub> sample surface with synthetic peak models consisting of decomposed components representing the contributions from individual chemical and spin states.



**Figure S4.** EDS spectrum of the MAPbBr<sub>3</sub> crystal (black) with the Pb (blue) and Br (red) X-ray lines for reference.

Table S1. Elemental composition of the MAPbBr<sub>3</sub> crystal determined by EDS.

Element	At %
С	50.1
N	10.6
Pb	9.6
Br	28.6
О	1.1

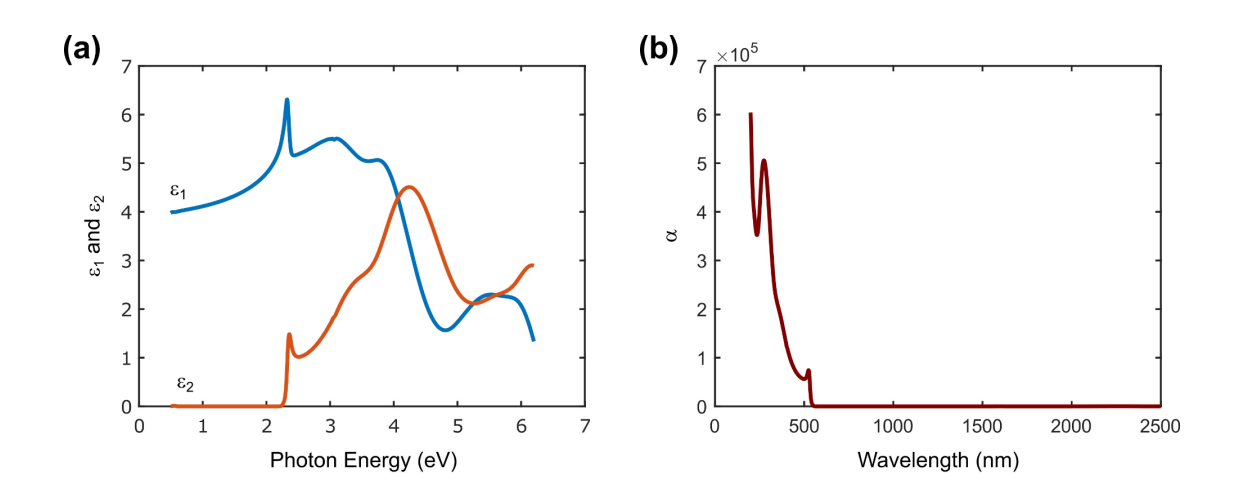


Figure S5. Dielectric functions (a) and absorption coefficient (b) for single crystal MAPbBr<sub>3</sub>.